International Journal of Minerals, Metallurgy and Materials
Volume 30, Number 9, September 2023, Page 1748
https://doi.org/10.1007/s12613-023-2631-8

Influences of oxide content and sintering temperature on microstructures and mechanical properties of intragranular-oxide strengthened iron alloys prepared by spark plasma sintering

Deyin Zhang[1,2),✉], *Xu Hao*[1)], *Baorui Jia*[1)], *Haoyang Wu*[1)], *Lin Zhang*[1,2)], *Mingli Qin*[1,2),✉], *and Xuanhui Qu*[1)]

1) Institute for Advanced Materials and Technology, University of Science and Technology Beijing, Beijing 100083, China
2) Shunde Innovation School, University of Science and Technology Beijing, Foshan 528399, China
(Received: 22 December 2022; revised: 14 March 2023; accepted: 15 March 2023)

Abstract: How to increase strength without sacrificing ductility has been developed as a key goal in the manufacture of high-performance metals or alloys. Herein, the double-nanophase intragranular yttrium oxide dispersion strengthened iron alloy with high strength and appreciable ductility was fabricated by solution combustion route and subsequent spark plasma sintering, and the influences of yttrium oxide content and sintering temperature on microstructures and mechanical properties were investigated. The results show at the same sintering temperature, with the increase of yttrium oxide content, the relative density of the sintered alloy decreases and the strength increases. For Fe–2wt%Y_2O_3 alloy, as the sintering temperature increases gradually, the compressive strength decreases, while the strain-to-failure increases. The Fe–2wt%Y_2O_3 alloy with 15.5 nm Y_2O_3 particles uniformly distributed into the 147.5 nm iron grain interior sintered at 650°C presents a high ultimate compressive strength of 1.86 GPa and large strain-to-failure of 29%. The grain boundary strengthening and intragranular second-phase particle dispersion strengthening are the main dominant mechanisms to enhance the mechanical properties of the alloy.

Keywords: oxide dispersion strengthening; spark plasma sintering; microstructure and properties; strengthening mechanism

1. Introduction

High strength, stiffness, and remarkable fracture toughness are the main requirements of structural materials in most engineering designs [1–4]. A long-standing problem for structural materials is how to increase strength while maintaining good ductility. Oxide dispersion strengthening has attracted great attention to enhance the mechanical properties of materials [5–10]. Due to outstanding strength, stiffness, and creep resistance, the oxide dispersion strengthened (ODS) iron-based alloys have been identified as a promising candidate for key components in the power, aerospace, and nuclear industries [11–16]. Homogeneously dispersed and ultrafine nanometric stable oxide particles in the matrix of the ODS alloys can act as effective obstacles against dislocation motion and grain boundary migration, which will contribute to further improvement of mechanical properties [17–21]. The related studies suggest that when second-phase particles in ODS alloys are uniformly dispersed within the matrix grains, it can become a reality to increase strength while maintaining good ductility [22–25]. On the contrary, if second-phase particles are located at the grain boundaries, they will act as stress concentrators to induce localized strains and promote crack formation, and thus the resultant ductility is inadequate [23,25]. Typically, ODS alloys are manufactured by powder metallurgy, involving mechanical alloying and subsequent hot consolidation, such as hot isostatic pressing, hot extrusion, or spark plasma sintering (SPS). The second-phase particles in ODS alloys prepared by solid–liquid or solid–solid mixture synthesis processes usually tend to be located at the grain boundaries, while the liquid–liquid blends route can achieve the uniform dispersion of second-phase particles into the grain interior [23]. In addition, it is well known that compared with other consolidation techniques, SPS can provide a much shorter sintering time and higher heating rate, which can effectively suppress grain growth, to obtain high performance ODS alloys [19,25–27]. In our previous investigation [28], we demonstrated a technique involving the solution combustion process and subsequent SPS to fabricate intragranular-oxide strengthened iron alloy. However, the influence of oxide particle content and sintering parameters on the microstructure and properties of the alloy, distribution of oxide particles, and grain refinement mechanism are still unclear.

In this study, the effects of Y_2O_3 content and sintering temperature on the microstructure and mechanical properties

✉ Corresponding authors: Deyin Zhang E-mail: zhangdeyin@ustb.edu.cn; Mingli Qin E-mail: qinml@mater.ustb.edu.cn

of the iron alloys with uniformly nanosized Y_2O_3 dispersed into the grain interior were investigated in detail, and the grain refinement, strengthening mechanism, and oxide particle distribution were also discussed.

2. Experimental

2.1. Materials preparation

Fe–Y_2O_3 nanocomposite powders with different Y_2O_3 contents were prepared by solution combustion synthesis and subsequent hydrogen reduction using raw materials including ferric nitrate ($Fe(NO_3)_3 \cdot 9H_2O$, 80.8 g), glycine ($C_2H_5NO_2$, 15.0 g), and yttrium nitrate ($Y(NO_3)_3 \cdot 6H_2O$), respectively. Among them, the addition amounts of $Y(NO_3)_3 \cdot 6H_2O$ were 0, 0.2wt%, 0.5wt%, 1.0wt% and 2.0wt% of Y_2O_3 in the synthesized nanocomposite powder, respectively. All raw materials with analytical reagent grade were commercially available.

All the above raw materials were dissolved in deionized water to prepare the mixture solution under continuous stirring. The as-prepared solution was placed on an electric furnace with controllable temperature and then heated in air. As heating proceeded, the solution with the evaporation of water gradually condensed into a reddish-brown gel. Then, the gel swelled dramatically, ignited suddenly, and burned violently with the release of a large number of gases. The entire process took only a few minutes, and as a result, a puffy porous combustion product was obtained. Subsequently, the as-synthesized product was carried out in a tube furnace at 400°C for 2 h under flowing hydrogen, forming the Fe–Y_2O_3 nanocomposite powders resulted.

The synthesized Fe–Y_2O_3 nanocomposite powders were uniaxial compaction to prepare the green compacts with a diameter of 15 mm by using a steel die under 300 MPa pressure holding for 2 min. The green compacts were then treated at 600°C for 2 h in a tube furnace under flowing hydrogen atmosphere with a gas flow of 1 L/min. The treated compacts were put into carbide molds at 600, 650, 700, and 800°C for SPS in vacuum atmosphere with the sintering pressure of 50 MPa for 5 min and the heating rate of 100°C/min. As the furnace was cooled to room temperature, the sintered compacts were created. Schematic of fabrication of Fe–Y_2O_3 alloy is presented in Fig. 1. The as-prepared Fe–Y_2O_3 alloys with 0, 0.2wt%, 0.5wt%, 1.0wt%, and 2.0wt% of Y_2O_3 were designated as sFe, sFeY2, sFeY5, sFeY10, and sFeY20, respectively.

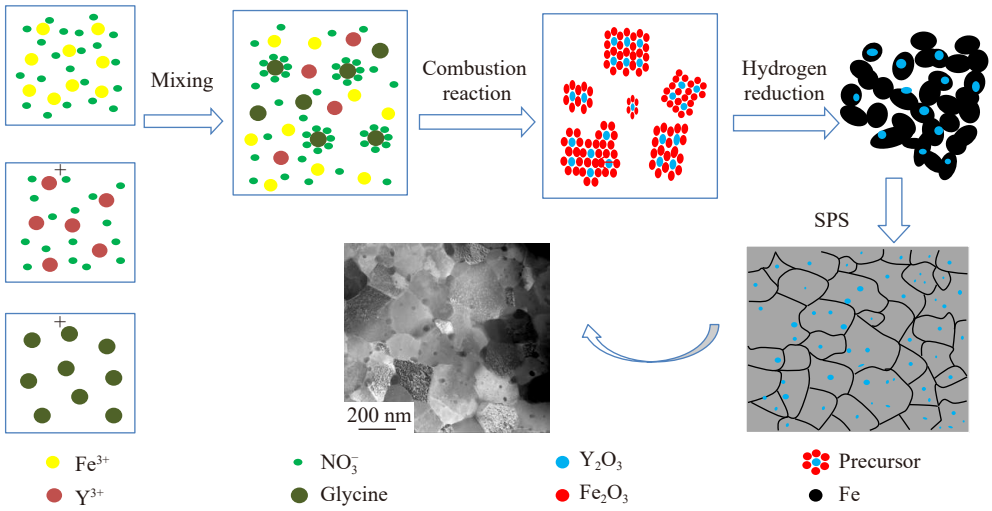

Fig. 1. Schematic of fabrication of Fe–Y_2O_3 alloy.

2.2. Materials characterization

Sample density was measured using the Archimedes method with at least five measurements. The Vickers microhardness test of the compact with at least 10 readings on random spots was performed on a Leica MH-6 microhardness tester under a 1.96 N loading with a duration of 15 s. The TEM (transmission electron microscopy) foils from the compact was prepared by a focused ion beam (FIB, Model). The morphology and microstructure of samples were analyzed by Tecnai G2 F30 S-TWIN TEM, equipped with an energy dispersive spectrometer (EDS). The grain size was evaluated using the image analysis software. The compression test was conducted at room temperature with a strain rate of 10^{-4} s^{-1} using an Instron 5982 electronic universal testing machine.

3. Results and discussion

Fig. 2 shows curves of the relative densities of Fe alloys with various Y_2O_3 contents obtained at different sintering temperatures. It can be clearly observed that when the sintering temperature is 600°C, the relative densities of sFe, sFeY2, sFeY5, sFeY10, and sFeY20 all reach or exceed 95%, which are 96.8%, 96.5%, 96.3%, 95.8%, and 95.0%, respectively. This result indicates that SPS is beneficial for nanocomposite powders to obtain high densities at relatively low sintering temperature, reflecting the fast densification characteristics. As the sintering temperature increases, the relative density increases gradually. When the sintering temperature rises to a certain level, the relative density increases slightly with the temperature continuing to increase. With the

sintering temperature increasing to 800°C, the relative densities of sFe, sFeY2, sFeY5, sFeY10, and sFeY20 reach 98.9%, 98.7%, 98.5%, 98%, and 96.7%, respectively. At the same sintering temperature, with the increase of the Y_2O_3 content, the relative density gradually decreases. Overall, the addition of the Y_2O_3 hinders the atomic diffusion and grain boundary migration in the sintering [24,29]. Therefore, when the Y_2O_3 content is excessive, the densification of nanocomposite powder becomes difficult. The high sintering energy of SPS enables the sintering, where the dispersed Y_2O_3 nanoparticles are migrated over or even swallowed by the grain boundary. In addition, the Fe–Y_2O_3 nanocomposite powder has the driving force of intrinsic excess surface energy, and the increase of Y_2O_3 nanoparticles highlights the refining effect of nanocomposite powder [30–31]. Therefore, the densification behavior of Fe–Y_2O_3 nanocomposite powders can be attributed to the combined effect of Y_2O_3 nanoparticles on the migration hindrance to grain boundaries and the refinement of composite powders.

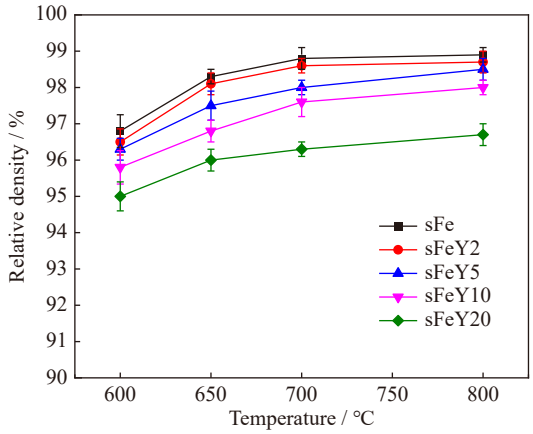

Fig. 2. Curves of the relative densities of Fe alloy with different Y_2O_3 contents varies at different sintering temperature.

Fig. 3 displays the microhardness of Fe alloy with different Y_2O_3 contents obtained at various sintering temperatures. It can be noticed that the microhardness of the sFe, sFeY2, sFeY5, sFeY10, and sFeY20 is $HV_{0.2}$ 298.0, 373.5, 391.9, 529.4, and 570.2, respectively, at a sintering temperature of 600°C. With the increase of sintering temperature, the microhardness gradually decreases. When the sintering temperature rises to 800°C, the microhardness of the sFe, sFeY2, sFeY5, sFeY10, and sFeY20 are $HV_{0.2}$ 203.9, 272.5, 304.4, 358.5, and 415.2, respectively. The higher temperature promotes the growth and aggregation of second phase particles and grain, and thus the grain refinement strengthening effect weakens, resulting in a lower microhardness. Moreover, the higher Y_2O_3 content has a stronger hindering effect on the growth of iron grains, which is beneficial to obtain a fine grain microstructure, resulting in higher microhardness.

To further verify the mechanical properties of the sintered alloy, the sintered alloy with 2wt% Y_2O_3 was selected to characterize its compressive properties. Stress–strain curves of Fe–2wt%Y_2O_3 alloys obtained at various sintering temperatures are displayed in Fig. 4. It is noticed that Fe–2wt%Y_2O_3 alloys sintered at 600°C exhibits a large ultimate compressive and yield strength of 2.12 and 1.96 GPa respectively, while the strain-to-failure is only 8%. With the sintering temperature increasing, the ultimate compressive and yield strengths decrease, the strain-to-failure increases. When the sintering temperature reaches 650°C, the ultimate compressive and yield strengths of Fe–2wt%Y_2O_3 alloys are 1.86 and 1.75 GPa respectively, and the strain-to-failure reaches 29%. As the sintering temperature rises to 700°C, the ultimate compressive and yield strengths of Fe–2wt%Y_2O_3 alloys drop to 1.52 and 1.29 GPa respectively, and the strain-to-failure becomes 54%. With the sintering temperature further rising to 800°C, Fe–2wt%Y_2O_3 alloys has a yield strength of 1.10 GPa, and no fracture occurs during the experimental compression process. The results show that the sintering temperature is a crucial factor affecting the properties of the alloy. With the increase of sintering temperature, the average grain size of the sintered alloy gradually increases, and the grain refinement strengthening effect gradually weakens, resulting that ultimate compressive and yield strengths decrease and the strain-to-failure increases.

TEM images of Fe–2wt%Y_2O_3 alloys obtained at various sintering temperatures are shown in Fig. 5. It is clearly observed that the Fe–Y_2O_3 alloys obtained at various sintering temperatures all exhibit equiaxed grains with the uniform

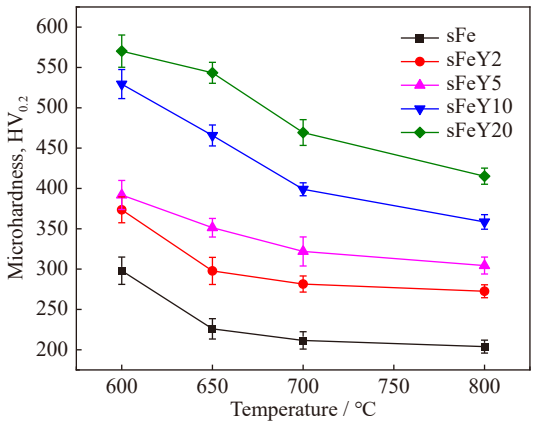

Fig. 3. Curves of the microhardness of Fe alloy with different Y_2O_3 contents at different sintering temperatures.

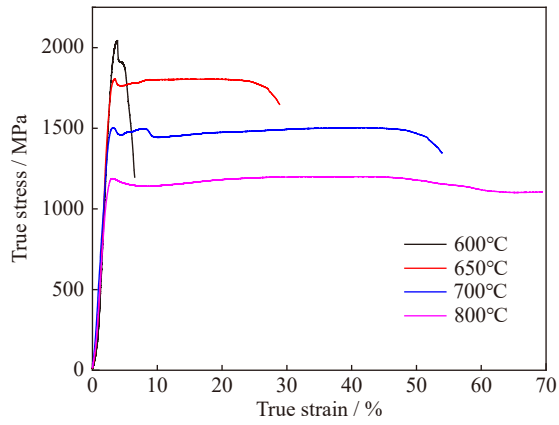

Fig. 4. Stress–strain curves of Fe–2wt%Y_2O_3 alloys sintered at various temperatures.

second-phase particles dispersed into the grains. Fig. 5(e) displays the EDS analysis of the second-phase particle marked by the open arrow in Fig. 5(d). The results show the Y and O elements are the main components of the particles. For more details, the high-resolutional TEM (HRTEM) image of Fe–2wt%Y_2O_3 alloys sintered at 650°C is presented in Fig. 5(f). It can be noticed that the interplanar spacings (d) are measured to be ~0.306 and 0.203 nm, in agreement with the lattice spacing of the (222) and (110) planes of cubic-Y_2O_3 and Fe, respectively. The results confirm that the second-phase particle is Y_2O_3, which is uniformly distributed inside the Fe grains.

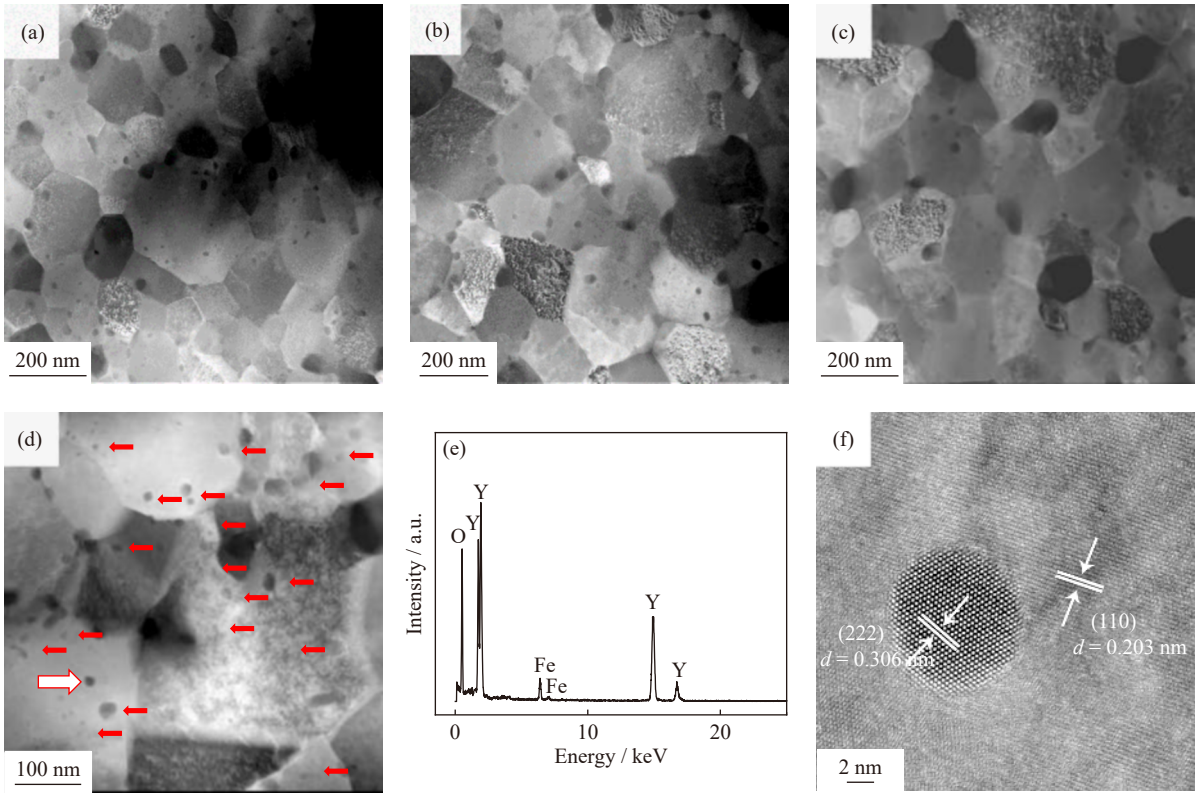

Fig. 5. Microstructure of Fe–2wt%Y_2O_3 alloys sintered at various temperatures: (a) TEM dark-field image at 600°C; (b, d) TEM dark-field image at 650°C; (c) TEM dark-field image at 700°C; (e) EDS analysis of the oxide particle and (f) HRTEM image the oxide particle marked by the open arrow in (d).

The size distributions of matrix grain and Y_2O_3 nanoparticles of Fe–2wt%Y_2O_3 alloys sintered at various temperatures are displayed in Fig. 6. The Fe–2wt% Y_2O_3 alloys sintered at 600°C has an average grain size of 119.6 nm with the Y_2O_3 particle size of 11.6 nm. The sizes of matrix grains and Y_2O_3 particles gradually increase with sintering temperature. As the sintering temperature reaches 650 or 700°C, the average grain size of the alloy reaches 147.5 or 178.7 nm, respectively, along with the oxide particle size of 15.5 or 19.6 nm. The results show that the shorter sintering time and lower sintering temperature during SPS process as well as the hindrance of the oxide particles can suppress the grain growth to form ultrafine grain microstructure.

Generally, in the second-phase dispersion-strengthened material, if the particle size and volume fraction of the second-phase are known, the limit grain size at which the grains stop growing can be predicted. The limiting grain size G_{crit} can be expressed as

$$G_{crit} = \frac{4r}{3f} \tag{1}$$

where f and r are the volume fraction and size of the second-phase particles, respectively [32–33]. Therefore, in order to achieve grain minimization, it is necessary to reduce the particle size or increase the volume fraction of the second-phase particles. The increase of the second-phase content will increase the difficulty of sintering and cost, and it is impossible to increase indefinitely. For a certain composition of materials, the reduction of the second-phase particle size becomes the only available way to reduce the grain size. Grain growth is achieved by grain boundary (GB) movement, and the second-phase particles inhibit grain growth by affecting GB mobility, thereby achieving grain refinement [34]. The pinning force (Zener-force) of the second-phase particles can be calculated from the GB area reduction caused by the intersection of the second-phase with the GB. For a planar GB and a spherical second-phase particle with radius r in contact with it, the maximum pinning force per particle (f^*) can be given as [32–34]:

$$f^* = 2\pi r\sigma \tag{2}$$

where σ represents the surface tension of the GB. The critical driving force of grain growth (ΔF^{crit}) can be expressed by:

$$\Delta F^{crit} = f^* \cdot n = 2\pi r\sigma \cdot n \tag{3}$$

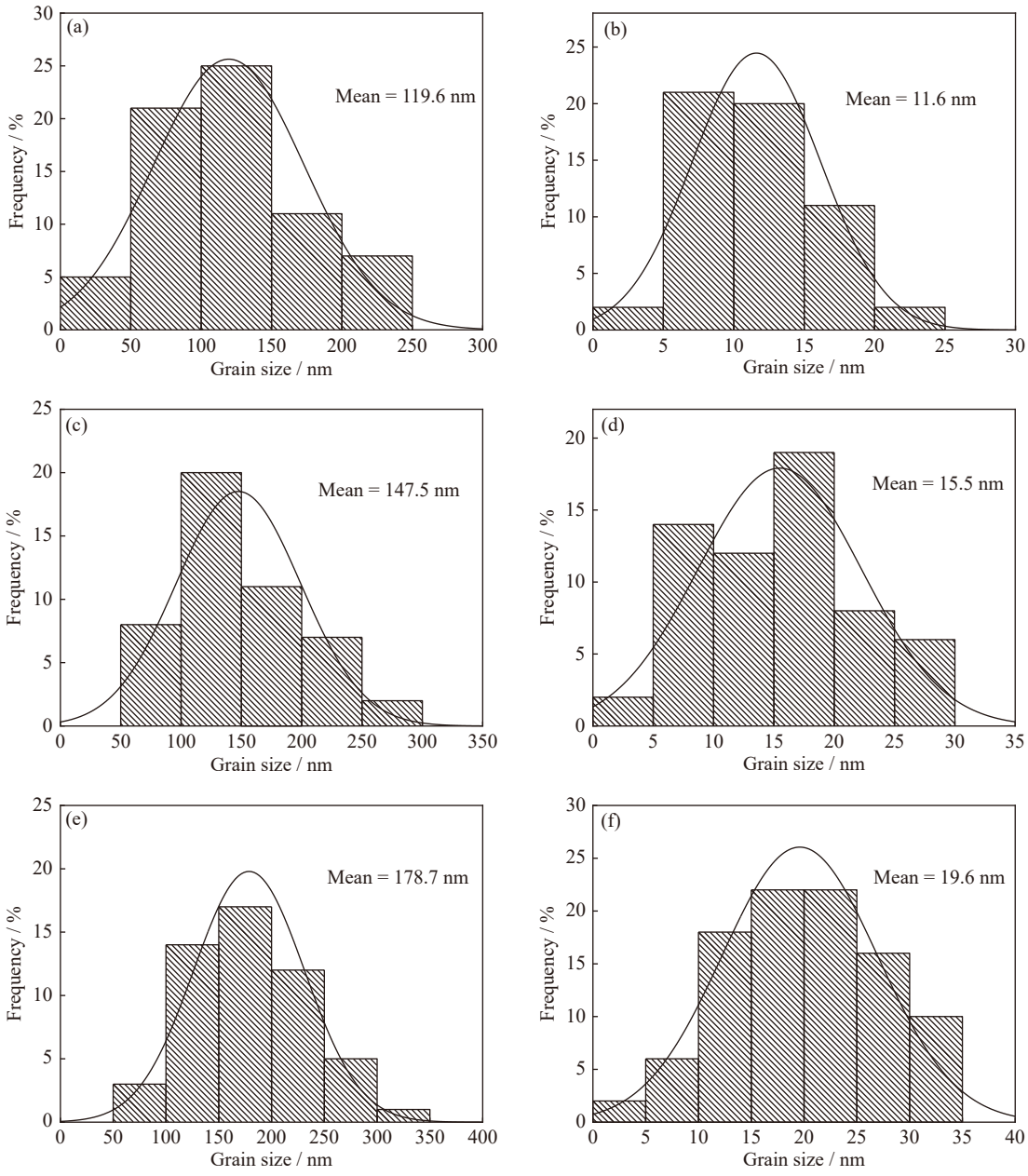

Fig. 6. Distribution of (a, c, e) Fe matrix grain sizes and (b, d, f) the corresponding oxide nanoparticles grain sizes of Fe–2wt%Y_2O_3 alloys sintered at various temperatures (a, b) 600°C; (c, d) 650°C; (e, f) 700°C.

where n is the second-phase particles number at the GB per unit area. When the driving force ΔF reaches the ΔF^{crit}, the GB will detach from the second-phase particles, leaving the second-phase particles inside the grain [33–35]. When the sintering conditions is determined, the ΔF of the grain growth is constant. The smaller the second-phase particles size, the smaller the ΔF^{crit}, and the easier that the second-phase particles enter the grain interior. Additionally, it is noted that during hot consolidation, the externally applied stress remarkably increases ΔF value, further promoting that the moving GBs detach from the particles.

The second-phase particle size also markedly affects the mobility of GBs and particles, and consequently the detachment of the second-phase particles from GBs [34,36]. For a spherical second-phase particle with radius r_p, the mobility (m_p) is limited by the interface diffusion, which can be given by [35]:

$$m_p\left(r_p\right) = \frac{\rho_s D_s \Omega^2}{\pi r^4 kT} \tag{4}$$

where ρ_s is the atoms surface density, D_s is the surface diffusion constant, Ω is the atomic volume, T is the absolute temperature, and k is Boltzmann constant. The velocity of a planar GB (v_{GB}) can be given by [35–36]:

$$v_{GB} = \frac{\Delta F \cdot m_b}{1 + \int_0^{\infty} \frac{\bar{n}\left(r_p\right) m_b}{m_p\left(r_p\right)} \mathrm{d}r_p} \tag{5}$$

where m_b is the GB mobility, $\int_0^{\infty} \bar{n}\left(r_p\right) \mathrm{d}r_p$ is the total number of particles per unit area. To estimate the effect of second-phase mobility on GB motion, the v_{GB} can be divided into the following two-limiting cases [34–36]:

$$v_{GB} \cong \begin{cases} \Delta F \cdot m_b, \int_0^\infty \frac{\bar{n}(r_p) m_b}{m_p(r_p)} dr_p \ll 1 \\ \frac{\Delta F \cdot m_p(r_p)}{\int_0^\infty \bar{n}(r_p) dr_p}, \int_0^\infty \frac{\bar{n}(r_p) m_b}{m_p(r_p)} dr_p \gg 1 \end{cases} \quad (6)$$

where $\int_0^\infty \frac{\bar{n}(r_p) m_b}{m_p(r_p)} dr_p \ll 1$ is corresponding to the high particle mobility of the second-phase particle, in which case, v_{GB} is equal to the GB velocity without the particles pinning. When $\int_0^\infty \frac{\bar{n}(r_p) m_b}{m_p(r_p)} dr_p \gg 1$, corresponding to the low particle mobility, v_{GB} is determined by the mobility of the second-phase particles. According to Eq. (4), the second-phase mobility is greatly affected by particle size, and decreases sharply with increasing particle size. The size and number of the second-phase particles will greatly affect the GB moving speed, thus affecting the grain growth. Herein, due to the nanoscale and high content of the Y_2O_3 particles, the inhibitory effect on grain growth is obvious. Consequently, the obtained Fe–Y_2O_3 alloys with Y_2O_3 dispersed into the grain interior still maintains a microstructure of ultrafine grains.

To further explore the strengthening mechanism of the alloy, the yield strength (σ_Y) of as-fabricated Fe–2wt%Y_2O_3 alloy can be expressed by [23,30,33]:

$$\sigma_Y = \sigma_0 + \Delta\sigma_i + \Delta\sigma_{GB} \quad (7)$$

where σ_0 is the inherent Peierls-Nabarro force of materials, which is lattice-friction stress for the dislocations (the Peierls-Nabarro force of Fe is ~28 MPa [30]), $\Delta\sigma_{GB}$ is the strength increased by grain boundary strengthening, and $\Delta\sigma_i$ is the strength increased by intragranular dispersed strengthening of the second-phase particles. The $\Delta\sigma_{GB}$ is given by the Hall-Petch equation:

$$\Delta\sigma_{GB} = \frac{K_0}{\sqrt{D}} \quad (8)$$

where D and K_0 are the average grain size and Hall-Petch constant (the Hall-Petch constant of Fe is 7.8 GPa·nm$^{-1/2}$ [37]), respectively. The $\Delta\sigma_i$ can be given by [23]:

$$\Delta\sigma_i = \Delta\sigma_{intra} = \frac{\phi G \boldsymbol{b}}{\lambda_{intra}} = \frac{\phi G \boldsymbol{b}}{d_{intra}} \left(\frac{6 f_{intra}}{\pi} \right)^{1/3} \quad (9)$$

where ϕ is a constant of order of 2, G and $\boldsymbol{b}$ are the shear modulus (the value of 82 GPa [31]) and the Burgers vector (the value of 0.25 nm [31]) of the Fe, respectively, f_{intra} (converted by the mass fraction) and d_{intra} are volume fraction and average particle size of the intragranular oxide particles, λ_{intra} (estimated by the average particle size and volume fraction) is interparticle spacing of the intragranular oxide particles. The calculation results are presented in Fig. 7. It can be clearly observed that intragranular second-phase particle dispersion strengthening and grain boundary strengthening are the main dominant mechanisms for the mechanical properties of the alloy. There are some deviations between the calculated values and the experimental results, which may be attributed to the change of the volume fraction of the second-phase particles, or the neglect of strengthening effect of few intergranular particles. Owing to the double-nanophase microstructure of intragranular-oxide strengthened iron alloy, the second-phase oxide particles can increase the resistance of GB migration, hinder the growth of matrix grains, and thus improve the strength of the alloy by fine-grain strengthening. At the same time, the uniform dispersion of the second-phase oxide particles into the grains can act as pinning, storing, accumulating, and hindering the migration of dislocations, which facilitates maintaining work hardening and homogeneous elongation, resulting in the alloys with high strength and remarkable toughness.

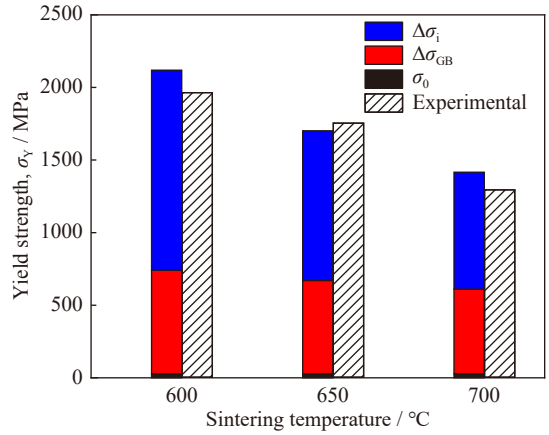

Fig. 7. Comparison of the calculated and experimental values of yield strength of Fe–2wt%Y_2O_3 alloys at various sintering temperatures.

4. Conclusion

In conclusion, we have successfully designed and fabricated the double-nanophase intragranular yttrium oxide dispersion strengthened iron alloy with high strength and appreciable ductility by SPS using the as-synthesized Fe–Y_2O_3 nanocomposites by solution combustion route. The relative densities of the alloys with different Y_2O_3 contents sintered at 600°C all reach or exceed 95%, and with the Y_2O_3 content increasing, the relative density gradually decreases, while microhardness gradually increases. The relative density of the alloy increases with sintering temperature, while the microhardness decreases. Compression test results and microstructure of the Fe–2wt%Y_2O_3 alloys show that higher sintering temperature increases the average grain size, resulting in lower compressive strength and higher strain-to-failure. The Fe–2wt%Y_2O_3 alloy sintered at 650°C with 15.5 nm Y_2O_3 particles uniformly distributed into the 147.5 nm iron grain interior achieves a suitable ultimate compressive strength of 1.86 GPa and strain-to-failure of 29%. The intragranular second-phase particle dispersion strengthening and grain boundary strengthening are the main dominant mechanisms for the enhancement of the alloy properties. Our strategy achieves the fabrication of a double-nanophase iron alloy with intragranular-oxide particles uniform dispersion, and

will provide a promising way for the design and manufacture of other ODS materials with excellent strength and ductility.

Acknowledgements

This work was financially supported by the Guangdong Basic and Applied Basic Research Foundation, China (No. 2021A1515110202), the Natural Science Foundation Program of Beijing, China (Nos. 2224104, 2202031, 2174079, and 2162027), the National Natural Science Foundation Program of China (Nos. 52131307, 52130407, 52071013, 52104359, 51774035, and 52174344), the Scientific and Technological Innovation Foundation of Foshan, China (No. BK21BE007), the National Key Research and Development Program of China (Nos. 2021YFB3701900, 2022YFB3705400, and 2022YFB3708800), the Beijing Municipal Science & Technology Commission, Administrative Commission of Zhongguancun Science Park, China (No. Z221100005822001), the S&T Program of Hebei, China (No. 20311001D), and the Fundamental Research Funds for the Central Universities (Nos. FRF-IDRY-20-022, FRF-TP-20-032A2, FRF-TP-20-100A1Z, and FRF-IDRY-22-030).

Conflict of Interest

Xuanhui Qu and Lin Zhang are the editorial board member and the youth editorial board member for this journal, respectively, and were not involved in the editorial review or the decision to publish this article. The authors declare that they have no known competing financial interests or personal relationships that could have appeared to influence the work reported in this paper.

References

[1] D. Raabe, C.C. Tasan, and E.A. Olivetti, Strategies for improving the sustainability of structural metals, *Nature*, 575(2019), No. 7781, p. 64.

[2] X.Y. Li and K. Lu, Improving sustainability with simpler alloys, *Science*, 364(2019), No. 6442, p. 733.

[3] Z.F. Lei, X.J. Liu, Y. Wu, *et al*., Enhanced strength and ductility in a high-entropy alloy via ordered oxygen complexes, *Nature*, 563(2018), No. 7732, p. 546.

[4] J. Bauer, M. Sala-Casanovas, M. Amiri, and L. Valdevit, Nanoarchitected metal/ceramic interpenetrating phase composites, *Sci. Adv.*, 8(2022), No. 33, art. No. eabo3080.

[5] L.P. Xie, W.Y. Sun, J.L. Wang, M.H. Chen, and F.H. Wang, Improving strength and oxidation resistance of a Ni-based ODS alloy *via in-situ* solid-state reaction, *Corros. Sci.*, 197(2022), art. No. 110078.

[6] E.M.O. Lahcen, M.M.Á. Alcázar, and C.P. Almeida, New high strength ODS Eurofer steel processed by mechanical alloying, *Mater. Sci. Eng. A*, 817(2021), art. No. 141288.

[7] L.Y. Yao, Y.J. Huang, Y.M. Gao, *et al*., Hot deformation behavior of nanostructural oxide dispersion-strengthened (ODS) Mo alloy, *Int. J. Refract. Met. Hard Mater*, 107(2022), art. No. 105881.

[8] N. Oono, S. Ukai, S. Kondo, O. Hashitomi, and A. Kimura, Irradiation effects in oxide dispersion strengthened (ODS) Ni-base alloys for Gen. IV nuclear reactors, *J. Nucl. Mater.*, 465(2015), p. 835.

[9] F.N. Xiao, T. Barriere, G. Cheng, *et al*., Extremely uniform nanosized oxide particles dispersion strengthened tungsten alloy with high tensile and compressive strengths fabricated involving liquid-liquid method, *J. Alloys Compd.*, 878(2021), art. No. 160335.

[10] J.H. Zhou, Y.F. Shen, and N. Jia, Strengthening mechanisms of reduced activation ferritic/martensitic steels: A review, *Int. J. Miner. Metall. Mater.*, 28(2021), No. 3, p. 335.

[11] A. Arora and S. Mula, Phase evolution characteristics, thermal stability, and strengthening processes of Fe–Ni based ODS invar steel produced by mechanical alloying and spark plasma sintering, *Mater. Sci. Eng. A*, 856(2022), art. No. 143972.

[12] P. Song, K. Yabuuchi, and P. Spätig, Insights into hardening, plastically deformed zone and geometrically necessary dislocations of two ion-irradiated FeCrAl(Zr)–ODS ferritic steels: A combined experimental and simulation study, *Acta Mater.*, 234(2022), art. No. 117991.

[13] P.K. Parida, A. Dasgupta, V. Srihari, *et al*., Structural investigations of Y_2O_3 dispersoids during mechanical milling and high-temperature annealing of Fe–15Y_2O_3–xTi (x = 0–15) model ODS alloys, *Adv. Powder Technol.*, 31(2020), No. 4, p. 1665.

[14] M. Brocq, B. Radiguet, J.M. Le Breton, F. Cuvilly, P. Pareige, and F. Legendre, Nanoscale characterisation and clustering mechanism in an Fe–Y_2O_3 model ODS alloy processed by reactive ball milling and annealing, *Acta Mater.*, 58(2010), No. 5, p. 1806.

[15] A. Mairov, D. Frazer, P. Hosemann, and K. Sridharan, Helium irradiation of Y_2O_3–Fe bilayer system, *Scripta Mater.*, 162(2019), p. 156.

[16] R.P. Li, L.J. Gong, J.G. Lin, J.X. Lin, K. Wang, and Z.M. Shi, Structural evolution of Fe–Y_2O_3–Ti powder during ball-milling and thermal treatment, *Ceram. Int.*, 45(2019), No. 16, p. 20011.

[17] S.J. Wu, J. Li, C.J. Li, Y.Y. Li, L.Y. Xiong, and S. Liu, Preliminary study on the fabrication of 14Cr–ODS FeCrAl alloy by powder forging, *J. Mater. Sci. Technol.*, 83(2021), p. 49.

[18] A. Hirata, T. Fujita, Y.R. Wen, J.H. Schneibel, C.T. Liu, and M.W. Chen, Atomic structure of nanoclusters in oxide-dispersion-strengthened steels, *Nat. Mater.*, 10(2011), No. 12, p. 922.

[19] S. Pasebani, A.K. Dutt, J. Burns, I. Charit, and R.S. Mishra, Oxide dispersion strengthened nickel based alloys via spark plasma sintering, *Mater. Sci. Eng. A*, 630(2015), p. 155.

[20] I. Hilger, F. Bergner, and T. Weißgärber, Bimodal grain size distribution of nanostructured ferritic ODS Fe–Cr alloys, *J. Am. Ceram. Soc.*, 98(2015), No. 11, p. 3576.

[21] J. Fu, T.P. Davis, A. Kumar, I.M. Richardson, and M.J.M. Hermans, Characterisation of the influence of vanadium and tantalum on yttrium-based nano-oxides in ODS Eurofer steel, *Mater. Charact.*, 175(2021), art. No. 111072.

[22] Z. Dong, Z.Q. Ma, J. Dong, *et al*., The simultaneous improvements of strength and ductility in W–Y_2O_3 alloy obtained via an alkaline hydrothermal method and subsequent low temperature sintering, *Mater. Sci. Eng. A*, 784(2020), art. No. 139329.

[23] G. Liu, G.J. Zhang, F. Jiang, *et al*., Nanostructured high-strength molybdenum alloys with unprecedented tensile ductility, *Nat. Mater.*, 12(2013), No. 4, p. 344.

[24] D.Y. Zhang, T. Wu, B.R. Jia, *et al*., Properties of intragranular-oxide-strengthened Fe alloys fabricated by a versatile facile and scalable route, *Powder Technol.*, 384(2021), p. 9.

[25] L. Huang, L. Jiang, T.D. Topping, *et al., In situ* oxide dispersion strengthened tungsten alloys with high compressive strength and high strain-to-failure, *Acta Mater.*, 122(2017), p. 19.

[26] V. Mihalache, I. Mercioniu, A. Velea, and P. Palade, Effect of the process control agent in the ball-milled powders and SPS-consolidation temperature on the grain refinement, density and Vickers hardness of $Fe_{14}Cr$ ODS ferritic alloys, *Powder Techn-*

ol., 347(2019), p. 103.
[27] A. Meza, E. Macía, P. Chekhonin, *et al*., The effect of composition and microstructure on the creep behaviour of 14 Cr ODS steels consolidated by SPS, *Mater. Sci. Eng. A*, 849(2022), art. No. 143441.
[28] M.L. Qin, D.Y. Zhang, G. Chen, *et al*., A double-nanophase intragranular-oxide-strengthened iron alloy with high strength and remarkable ductility, *Metall. Mater. Trans. A*, 50(2019), No. 3, p. 1103.
[29] J. Besson and A.G. Evans, The effect of reinforcements on the densification of a metal powder, *Acta Metall. Mater.*, 40(1992), No. 9, p. 2247.
[30] B. Srinivasarao, K. Oh-ishi, T. Ohkubo, and K. Hono, Bimodally grained high-strength Fe fabricated by mechanical alloying and spark plasma sintering, *Acta Mater.*, 57(2009), No. 11, p. 3277.
[31] R. Vijay, M. Nagini, J. Joardar, M. Ramakrishna, A.V. Reddy, and G. Sundararajan, Strengthening mechanisms in mechanically milled oxide-dispersed iron powders, *Metall. Mater. Trans. A*, 44(2013), No. 3, p. 1611.
[32] C.S. Smith, Grains, phases, and interfaces: An interpretation of microstructure, *Trans. Metall. Soc. AIME*, 175(1948), p. 15.
[33] M.L. Qin, J.J. Yang, Z. Chen, *et al*., Preparation of intragranular-oxide-strengthened ultrafine-grained tungsten via low-temperature pressureless sintering, *Mater. Sci. Eng. A*, 774(2020), art. No. 138878.
[34] L. Jiang, H.M. Wen, H. Yang, *et al*., Influence of length-scales on spatial distribution and interfacial characteristics of B_4C in a nanostructured Al matrix, *Acta Mater.*, 89(2015), p. 327.
[35] G. Gottstein and L.S. Shvindlerman, Theory of grain boundary motion in the presence of mobile particles, *Acta Metall. Mater.*, 41(1993), No. 11, p. 3267.
[36] Z. Chen, M.L. Qin, J.J. Yang, L. Zhang, B.R. Jia, and X.H. Qu, Thermal stability and grain growth kinetics of ultrafine-grained W with various amount of La_2O_3 addition, *Metall. Mater. Trans. A*, 51(2020), No. 8, p. 4113.
[37] R. Vijay, M. Nagini, S.S. Sarma, M. Ramakrishna, A.V. Reddy, and G. Sundararajan, Structure and properties of nano-scale oxide-dispersed iron, *Metall. Mater. Trans. A*, 45(2014), No. 2, p. 777.